electronics

Article

Load Modulation Feedback in Adaptive Matching Networks for Low-Coupling Wireless Power Transfer Systems

Michele Bertozzi [1,*], Alessandro Catania [1], Gabriele Bandini [2], Sebastiano Strangio [1] and Giuseppe Iannaccone [1]

[1] Department of Information Engineering, University of Pisa, 56126 Pisa, Italy; alessandro.catania@unipi.it (A.C.); sebastiano.strangio@unipi.it (S.S.); giuseppe.iannaccone@unipi.it (G.I.)
[2] Department DESTeC, University of Pisa, 56126 Pisa, Italy; gabriele.bandini@ing.unipi.it
* Correspondence: michele.bertozzi@phd.unipi.it

Abstract: This paper explores the use of load modulation feedback (LMF) in adaptive matching networks (MN) for low-coupling inductive wireless power transfer systems, with an emphasis on its use in implantable medical devices. After deriving the handy expressions of link efficiency and modulation depth in the case of LMF in the case of loose coupling, a brief overview of the most common capacitive resonance networks is presented. In particular, the MN employing two capacitors in Series–Parallel and in Parallel–Series configurations allow adaptivity with a wide range of load conditions. Then, the authors describe an effective design procedure of an adaptive matching network with LMF for an inductive wireless power transfer system, exploring the trade-off between power efficiency and modulation depth. Analytical and electrical simulations show that the proposed simple modulation strategy can successfully achieve high power transfer efficiency while maintaining steady back telemetry under varying loading conditions.

Keywords: wireless power transfer; implantable medical devices; load modulation feedback; matching network

Citation: Bertozzi, M.; Catania, A.; Bandini, G.; Strangio, S.; Iannaccone, G. Load Modulation Feedback in Adaptive Matching Networks for Low-Coupling Wireless Power Transfer Systems. *Electronics* **2023**, *12*, 4619. https://doi.org/10.3390/electronics12224619

Academic Editor: Fabio Corti

Received: 12 October 2023
Revised: 2 November 2023
Accepted: 10 November 2023
Published: 12 November 2023

1. Introduction

Implantable medical devices (IMDs) are small devices that are surgically inserted into the human body to fulfill several objectives, such as the restoration of anatomical impairments, substitution of absent components, administration of medical treatments, and monitoring of physiological parameters [1]. These devices often embed essential electronic systems that require an energy source (commonly batteries) constrained by limitations on finite energy capacity, spatial requirements, and the potential inclusion of hazardous substances [2]. To overcome these issues, research studies have been directed towards the development of wireless power transfer (WPT) systems for IMDs, which are capable of continuously transmitting higher power levels compared with conventional batteries and extending the lifetime of the devices [3,4]. These systems can be implemented through various approaches, leveraging diverse physical phenomena including acoustic waves, lasers, and electromagnetic fields. One notable technology, known as inductive wireless power transfer, exploits electromagnetic fields to enable the transmission of power through the human body [5].

In this framework, the European Project AUTOCAPSULE seeks to demonstrate the feasibility of a technology platform for the early diagnosis of inflammatory bowel disease and bowel cancer through the development of an autonomous multimodal implantable endoscopic capsule (Figure 1). The capsule integrates a high-precision magnetic robotic positioning system to guide the capsule, a white-light imaging (WLI) system to acquire images of the gastrointestinal track, and a micro ultrasound array (micro US) to perform an in-depth tissue analysis. The platform is a wireless evolution of the magnetic manipulation system for gastrointestinal ultrasound [6]. White-light and micro US imaging systems are both power-hungry, in terms of instantaneous current consumption (mainly due to the high-voltage pulser needed to drive the US transducer [7]), as well as average current consumption (for white LED lighting or high-speed ADC for digitizing echoic signals [8]). The integration of these two subsystems represents a major challenge and poses strict requirements for the power sourcing of the endoscopy capsule. The WPT system of the capsule is a resonant inductive system that provides power to all subsystems, removing any constraints on the time usage and minimizing the volume occupation [9,10]. The WPT system is based on the inductive resonant coupling between a transmitter (Tx) coil, placed on the robotic arm used for the remote control of the capsule during the medical procedure and three orthogonal coils for the receiver (Rx), in order to address misalignment issues [11,12]. The compact size of the capsule requires a small Rx coil, resulting in a weak inductive coupling. Consequently, a substantial amount of energy is required by the Tx system to transfer the necessary power on the Rx side. However, it is crucial that the irradiated energy respects the Specific Absorption Rate (SAR) limits prescribed by law under any operating condition [13,14].

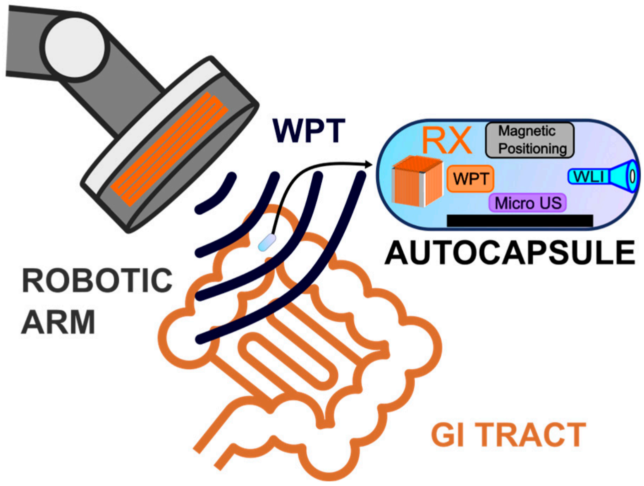

Figure 1. Example of application of implantable endoscopic capsule developed for the AUTOCAPSULE project.

To adhere to SAR limitations and control the transmitted power, especially in terms of average exposure limits, it is important that the capsule transmits back information on its power status. If the received power overcomes the power required by the capsule, it becomes crucial to reduce the transmitted power, thus limiting the radiation directed towards the human body and increasing the power efficiency of the system. Conversely, if the power demanded by the capsule increases or the coupling factor is reduced as a consequence of capsule movements, the Tx needs to know when to increase the transmitted power. The load modulation feedback (LMF) technique (also referred to as back telemetry or data telemetry) [15–17] is an effective method of transmitting information back from the Rx to the Tx side, without involving additional links (as, for example, in [18]). This is based on the modulation of the load seen by the Rx coil and the inductive coupling with the transmitting coil [19,20]. This modulation can be used to encode information related to the actual power status of the capsule and is detectable on the Tx side [21,22].

In this work, we provide a simple yet effective theoretical background for low-coupling inductive WPT. After deriving the handy analytical expressions of the link power efficiency (η) and the modulation depth (MD) of the LMF, we studied the most popular matching networks, highlighting the advantages of implementing load adaptivity. We also propose a straightforward and reliable design procedure for the Rx system in order to maximize the power efficiency needed in the presence of LMF to transmit information to regulate the Tx power. Though the proposed approach is general and can be implemented regardless of the specific matching network, we showed how the best trade-off between η and MD over a wide range of load can be achieved only employing adaptive matching networks and we confirmed the results in a specific case study by means of numerical and electrical simulations, also taking into account varying coupling coefficients to emulate the possible variations in distance and misalignment between Tx and Rx coils.

2. Theoretical Model

2.1. WPT Link

The analysis of WPT in inductive links has been extensively studied [10]. Here, we will briefly recap the most important results and draw some simplified expressions derived under low-coupling scenarios (coupling factor $k \ll 1$) typical of WPT systems for IMDs due to the small size of the receiving coil, the distance between Tx and Rx, and the presence of the human body. For instance, Ref. [11] shows by means of electromagnetic simulations that a coupling factor of 1×10^{-3} is achievable with a distance of 15 cm between Tx and Rx coil, with the latter designed to be 1 cm in size in order to fit into an endoscope capsule.

Figure 2a shows a typical representation of an inductive WPT link. On the Tx side, a resonance matching network (e.g., series resonance as depicted in the picture) is usually used to adapt the load impedance (the Tx coil) of the power amplifier. A simplified model of the Tx coil with only its self-inductance L_{TX} and its Equivalent Series Resistance (ESR) R_{TX} is used, considering an operating angular frequency ω_0 that is much lower than the self-resonance frequency of the coil. A typical parameter used to measure the efficiency of the coil is the quality factor, defined as

$$Q_{Tx} = \omega_0 L_{Tx} / R_{Tx} \tag{1}$$

The Rx side consists of the Rx coil, which is similarly modeled by means of the parameters L_{RX} and R_{RX}, with a quality factor:

$$Q_{Rx} = \omega_0 L_{Rx} / R_{Rx} \tag{2}$$

A passive MN between the Rx coil and the ac-dc converter (voltage rectifier) is usually used to reach both the resonance condition and the maximum power transfer. More details about the matching network will be given in Section 3. A generic load Z_L models the different circuits that can be powered by the WPT system. In typical IMDs, due to the complexity of the electronic parts, the load can be variable. The presence of the human body further reduces the performance of the inductive link due to the losses and the coupling effects; this can be easily modeled through a lumped resistor placed in series with the transmitter coil and a lumped capacitor placed in parallel to the Rx coil [23]. This parasitic capacitor will shift the resonance frequency of the Tx MN but can be compensated for by modifying C_{Tx} or through an adaptive MN [24]. The parasitic resistance, instead, can be embedded together with the ESR into an equivalent R_{TX} (without affecting the following theoretical discussion), resulting in a reduction in the equivalent Q_{Tx}.

It is convenient to define Z_{REF} as the reflected impedance that models the mutual coupling with the Rx side on the Tx side (Figure 2b). The impedance Z_{IN} seen by the input source can be easily evaluated by means of the Kirchhoff Laws. The voltage v_{IN} across the series of resonance capacitor and mutual coupled inductor is

$$v_{IN} = i_{Tx}\left(\frac{-j}{\omega_0 C_{Tx}} + R_{Tx} + j\omega_0 L_{Tx}\right) + j\omega_0 M i_{Rx} \tag{3}$$

where M is the mutual coupling coefficient between L_{Tx} and L_{Rx} and is related to the coupling factor k through the relationship

$$M = k\sqrt{L_{Tx} L_{Rx}} \tag{4}$$

The current i_{Rx} on the receiver side generated by the inductive coupling is

$$i_{Rx} = \frac{-i_{Tx} j\omega_0 M}{R_{Rx} + j\omega_0 L_{Rx} + Z_{MN}} \quad (5)$$

From the ratio of v_{IN} and i_{Tx}, it is straightforward to derive the input impedance Z_{IN} by exploiting Equations (3) and (4), separating the contribution due to the reflection of the Rx on the Tx side in the abovementioned Z_{REF}:

$$Z_{IN} = \frac{v_{IN}}{i_{Tx}} = \frac{-j}{\omega_0 C_{Tx}} + R_{Tx} + j\omega_0 L_{Tx} + Z_{REF} \quad (6)$$

$$Z_{REF} = \frac{\omega_0^2 k^2 L_{Tx} L_{Rx}}{R_{Rx} + j\omega_0 L_{Rx} + Z_{MN}} \quad (7)$$

It is worth noting that the variation in the impedance seen at the input of the matching network (Z_{MN}) causes a variation in the impedance Z_{IN} seen by the input voltage source through Z_{REF}, and consequently in the current flowing on the Tx side. Detecting this amplitude variation in the Tx current without affecting the performance of the link (i.e., by means of a small resistive shunt or an additional inductive coupling), information coded in the modulation of Z_{MN} can be transmitted back from the Rx side to the Tx side. This is the basic principle of the LMF technique, which will be further discussed in the following sections. In the following, we will consider the resonance condition on the Tx side at the operating angular frequency ω_0, which means that the input impedance consists only of the sum of R_{Tx} and Z_{REF}.

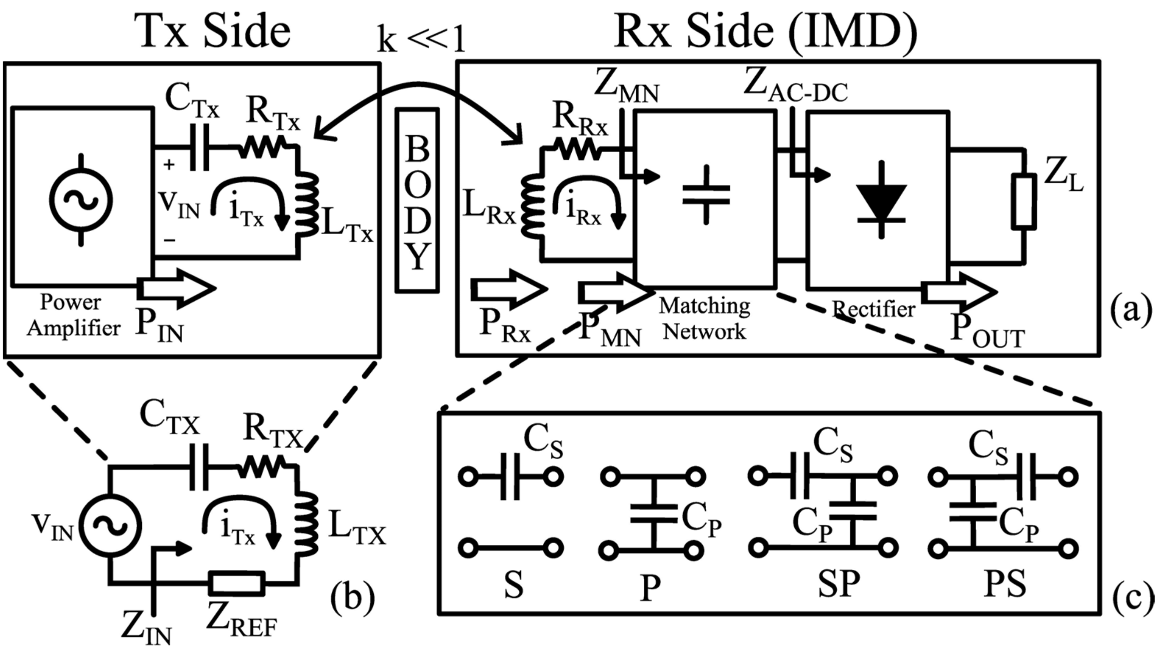

Figure 2. (**a**) Block diagram of inductive WPT system: the Tx side consists of a power amplifier and a series capacitor C_{TX} in resonance with the Tx coil L_{Tx} (R_{Tx} represents the ESR but can also model the equivalent resistance of the human body losses), while the Rx side (miniaturized in order to fit into the IMD) consists of an Rx coil L_{Rx} (and its ESR R_{Rx}), a capacitive matching network and an AC-DC converter, loaded by a generic impedance Z_L. (**b**) The equivalent Tx circuit with reflected impedance Z_{REF} can be used to study the inductive link efficiency. (**c**) Four possible matching network topologies on the Rx side have been analyzed, in the order, from left to right: Series, Parallel, Series–Parallel and Parallel–Series.

2.2. Power Efficiency

The overall power efficiency η_{Tot}, defined as the ratio between the output power delivered to the load P_L and the active power delivered by the voltage source P_{IN}, can be easily written as the product of three partial power efficiencies:

$$\eta_{Tot} = \frac{P_{OUT}}{P_{IN}} = \frac{P_{Rx}}{P_{IN}}\frac{P_{MN}}{P_{Rx}}\frac{P_{OUT}}{P_{MN}} = \eta_{Tx}\eta_{Rx}PCE \tag{8}$$

where PCE is the Power Conversion Efficiency of the rectifier, while η_{Tx} and η_{Rx} are, respectively, the ratio between the power received by Rx (P_{Rx}) and the input power and the ratio between the input power of the matching network (P_{MN}) and P_{Rx}. Considering that the PCE can be optimized using advanced circuit topologies [25] that are beyond the scope of this work, we will focus on the study of the link efficiency:

$$\eta_{link} = \eta_{Tx}\eta_{Rx} \tag{9}$$

where the two partial efficiencies are defined as

$$\eta_{Tx} = \frac{P_{Rx}}{P_{IN}} = \frac{Re\{Z_{REF}\}}{Re\{Z_{REF}\} + R_{Tx}} \tag{10}$$

$$\eta_{Rx} = \frac{P_{MN}}{P_{Rx}} = \frac{Re\{Z_{MN}\}}{Re\{Z_{MN}\} + R_{Rx}} \tag{11}$$

After conveniently defining the link potential,

$$X = k^2 Q_{Tx} Q_{Rx} \tag{12}$$

which sums up all the characteristics of the coils and the inductive coupling. It is quite straightforward to obtain an expression of the overall link efficiency that emphasizes its dependency on Z_{MN} [5]. Here, we will limit our research to a case study characterized by loose coupling and quality factors, such that the link potential $X \ll 1$. This scenario is of particular interest in WPT systems for implantable medical devices, where the Rx coil size, the distance between the coils and the presence of the human body limits the link potential to a few percent [26]. The reflected impedance Z_{REF} can be rewritten starting from Equation (4), highlighting its dependance by using the link potential and the real and imaginary parts of Z_{MN}:

$$Z_{REF} = R_{Tx}\frac{k^2\frac{\omega_0 L_{Tx}}{R_{Tx}}\frac{\omega_0 L_{Rx}}{R_{Rx}}}{\left(1+\frac{Re\{Z_{MN}\}}{R_{Rx}}\right) + j\left(Q_{Rx} + \frac{Im\{Z_{MN}\}}{R_{Rx}}\right)} = XR_{Tx}\frac{\left(1+\frac{Re\{Z_{MN}\}}{R_{Rx}}\right) - j\left(Q_{Rx} + \frac{Im\{Z_{MN}\}}{R_{Rx}}\right)}{\left(1+\frac{Re\{Z_{MN}\}}{R_{Rx}}\right)^2 + \left(Q_{Rx} + \frac{Im\{Z_{MN}\}}{R_{Rx}}\right)^2} \tag{13}$$

Using Equations (7), (9)–(12), it is possible to derive a simplified expression of the link efficiency:

$$\eta_{link} = \frac{P_{MN}}{P_{IN}} = \eta_{Tx}\eta_{Rx} \cong X\frac{Re\{Z_{MN}\}/R_{Rx}}{(1 + Re\{Z_{MN}\}/R_{Rx})^2 + (Q_{Rx} + Im\{Z_{MN}\}/R_{Rx})^2} \tag{14}$$

From now on, considering the direct proportionality with X, we will show only the normalized link efficiency η_{link}/X. It is easy to demonstrate that in low-coupling conditions, the maximum power (delivered to the load) point and the maximum efficiency point conditions are reached for the same value of $Z_{MN} = Z_{MN-opt}$. $Z_{MN\text{-}opt}$ is the complex conjugate of the source impedance, which is intended here as the impedance of the Rx coil; i.e., $Z_{MN\text{-}opt}$ is the value of impedance that allows at the same time the resonance condition on the Rx side ($Im\{Z_{MN}\} = -Q_{Rx}R_{Rx} = -\omega_0 L_{Rx}$) and the matched load condition ($Re\{Z_{MN}\} = R_{Rx}$); if both conditions are met, $\eta_{link-opt}/X = 0.25$.

2.3. Modulation Depth

Proper modulation of Z_{MN} between more phases and at different frequencies may allow the transmission of useful information from Rx to Tx, detected by means of coherent demodulation of the current on the Tx side. Indeed, the amplitude of the current flowing on the resonant Tx side in loose coupling conditions ($X \ll 1$) is

$$i_{Tx} = \frac{v_{IN}}{|Z_{IN}|} = \frac{v_{IN}}{|R_{Tx} + Z_{REF}|} \cong \frac{v_{in}}{R_{Tx}\sqrt{1+2y}} \tag{15}$$

$$y = X\frac{1 + Re\{Z_{MN}\}/R_{Rx}}{(1 + Re\{Z_{MN}\}/R_{Rx})^2 + (Q_{Rx} + Im\{Z_{MN}\}/R_{Rx})^2} \tag{16}$$

Let us consider a variation in the impedance seen at the input of the matching network on the Rx side between two phases: Z_{MN1} and Z_{MN2}. This will cause a variation in the amplitude of i_{Tx} proportional to the difference in the parameters y_2 and y_1 (depending on Z_{MN2} and Z_{MN1}, respectively):

$$\Delta i_{Tx} = \left|\frac{V_{IN}}{|Z_{IN2}|} - \frac{V_{IN}}{|Z_{IN1}|}\right| \cong \frac{V_{IN}}{R_{Tx}}|y_2 - y_1| \tag{17}$$

The modulation depth can be obtained by dividing the amplitude variation (12) by the amplitude of the Tx current (10) when no coupling is present:

$$MD = \frac{\Delta i_{Tx}}{i_{Tx}} \cong |y_2 - y_1| \tag{18}$$

It is worth remarking that these simplified expressions have been obtained under the assumption of $X \ll 1$, thus neglecting the term proportional to X^2 in Equation (10), truncating the series expansion to the first order in Equation (12), as well as the y term of i_{Tx} in Equation (13). Analogously to the link efficiency, from now on, we will show only the normalized modulation depth MD/X. The LMF introduces the obvious penalty of reducing the power efficiency of the link. In Section 4, we will study the trade-offs in terms of MD and the average link efficiency $\overline{\eta_{link}}$, defined as the mean value between η_{link1} and η_{link2} (each evaluated according to Equation (9) during each phase of the LMF).

3. Matching Networks

The analysis carried out so far is independent of the matching network topology employed on the Rx side but clearly highlights the requirements to maximize the power transfer: resonance with L_{Rx} and matched load with R_{Rx}. Considering that Z_{MN} depends on the input impedance of the rectifier $Z_{AC\text{-}DC}$, which in turn depends on Z_L, achieving both the specifications is challenging, especially under varying loading conditions. Four MN topologies (Figure 2c), usually referred to as resonant structures, are commonly used [27]: Series (S), Parallel (P), Series–Parallel (SP) and Parallel–Series (PS). In order to simplify the analysis, the matching networks are loaded by a generic R_L, instead of the rectifier input impedance. An analysis of the effect of $Z_{AC\text{-}DC}$ is given in [28]. Numerical and electrical simulations (by means of Spectre™ simulator) have been run to verify the validity of the proposed analytical models. The coil parameters, the coupling factor and the operating frequency used for the electrical simulations have been derived from Ref. [11], which shows the optimization of the WPT link through 3D FEM simulations for the AUTOCAPSULE project.

3.1. Series

This is the most straightforward implementation of the resonance network. The input impedance is simply:

$$Z_{MN} = R_L - \frac{j}{\omega_0 C_S} \tag{19}$$

The resonance condition is reached by choosing:

$$C_S = C_{RES} = 1/\left(\omega_0^2 L_{Rx}\right) = 1/(\omega_0 Q_{Rx} R_{Rx}) \tag{20}$$

However, since the matching network includes only one capacitor, the real part of Z_{MN} depends only on the value of R_L, which is usually variable. Figure 3a shows the normalized link efficiency against R_L/R_{Rx}; as expected, the maximum efficiency is reached for $R_L = R_{Rx}$, while the efficiency quickly drops when moving away from the optimum point.

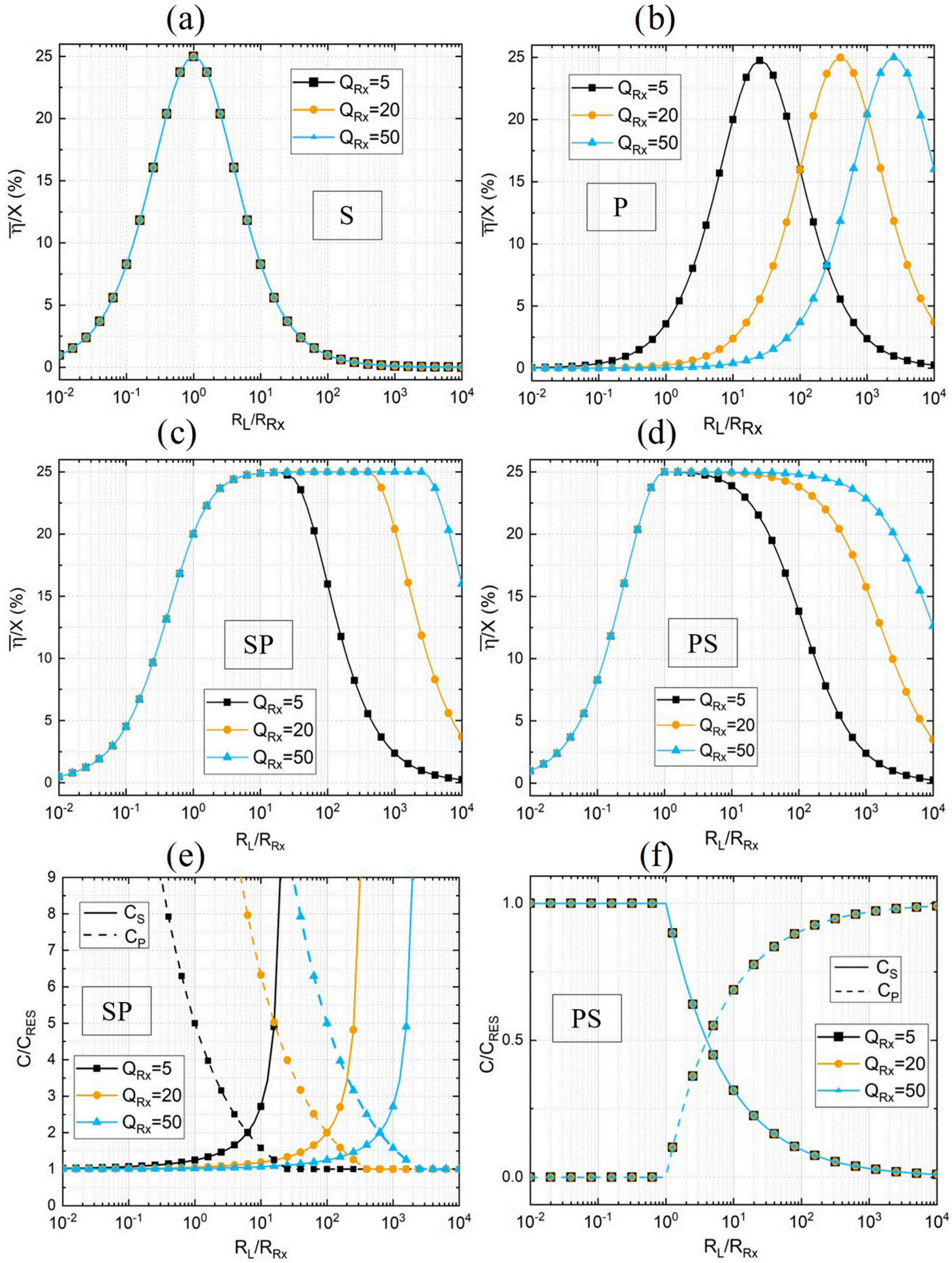

Figure 3. Normalized efficiency of (**a**) Series MN, (**b**) Parallel MN, (**c**) Series–Parallel MN and (**d**) Parallel–Series MN. Normalized Series and Parallel capacitances in (**e**) SP MN and (**f**) PS MN. All the simulations have been performed numerically and electrically (with $k = 1 \times 10^{-3}$) for three different values of the Rx coil quality factor.

3.2. Parallel

This is another very common topology, which presents an input impedance equal to

$$Z_{MN} = \frac{R_L}{1+\omega_0{}^2 R_L^2 C_P^2} - j\frac{\omega_0 R_L^2 C_P}{1+\omega_0{}^2 R_L^2 C_P^2} \tag{21}$$

Differently from the S topology, the resonance condition depends on R_L. Assuming that $\omega_0^2 R_L^2 C_P^2 \gg 1$, the resonance condition is reached, fixing the capacitor $C_P = C_{RES}$. As in the S topology, the matching condition still depend on the value of R_L, but differently from the previous case, maximum power transfer is reached for $R_L = Q_{Rx}^2 R_{Rx}$. Figure 3b shows the normalized link efficiency against R_L/R_{Rx} for different quality factors of the Rx coil. Comparing this behavior with that in Figure 3a, we can reach a first conclusion: the Series MN is desirable for heavy loads, while on the contrary, the Parallel MN is more efficient for light-load conditions.

3.3. Series–Parallel

In the previous topologies, the use of only one passive component in the resonance network does not allow the maximum theoretical efficiency under generic load conditions. The SP topology employs two capacitors and shows the following input impedance:

$$Z_{MN} = \frac{R_L}{1+\omega_0{}^2 R_L^2 C_P^2} - j\frac{1+\omega_0{}^2 R_L^2\, C_P(C_P+C_S)}{(1+\omega_0{}^2 R_L^2 C_P^2)\omega_0 C_S} \tag{22}$$

Both the real and the imaginary parts depend on R_L, but this time, there are two capacitors that can be tuned to reach at the same time the resonance and the matched load condition. If $\omega_0^2 R_L^2 C_P^2 \ll 1$, the matching network behaves as the S topology, while for $\omega_0^2 R_L^2 C_P^2 \gg 1$, we can simplify the expression of Z_{MN} and derive the two following design rules: (i) the resonance condition is met if $\left(C_P{}^{-1} + C_S{}^{-1}\right)^{-1} = C_{RES}$ and at the same time (ii) the matched load condition is met if $C_P = C_{RES} Q_{Rx}\sqrt{R_{Rx}/R_L}$. This is valid up to $R_L = R_{Rx} Q_{Rx}^2$; for this specific load value, the capacitor C_S tends to infinite, while C_P is equal to C_{RES}. For $R_L = R_{Rx} Q_{Rx}^2$, the optimal SP network collapses in a P one. The normalized link efficiency is plotted in Figure 3c for different Q_{Rx}. Compared with the previous case, a link efficiency close to the optimal one can be reached for a wide range of R_L. The optimal values of C_S and C_P needed to reach the maximum efficiency under different loading conditions are shown in Figure 3e for different quality factors.

3.4. Parallel–Series

The PS topology is analogous to the SP topology, still exploiting two capacitors but in a different configuration. The impedance shown by the matching network is

$$Z_{MN} = \frac{R_L\left(\frac{C_S}{C_S+C_P}\right)^2}{1+\omega_0{}^2 R_L^2 C_X^2} - j\frac{1+\omega_0{}^2 R_L^2\, C_S C_X}{(1+\omega_0{}^2 R_L^2 C_X^2)\,\omega_0(C_S+C_P)} \tag{23}$$

with $C_X = \left(C_P{}^{-1} + C_S{}^{-1}\right)^{-1}$. If $\omega_0^2 R_L^2 C_X^2 \gg 1$, the matching network behaves as the P one; while for $\omega_0^2 R_L^2 C_X^2 \ll 1$ and $\omega_0^2 R_L^2 C_P C_X \ll 1$, we can simplify the expression of Z_{MN} and obtain the following two rules for sizing CP and CS: (i) $(C_P + C_S) = C_{RES}$ for the resonance condition and then (ii) $C_S = C_{RES}\sqrt{R_{Rx}/R_L}$ for the matched load condition. This is valid for a range of loads down to R_{RX}, while for smaller loads, we can fix $C_S = C_{RES}$ and $C_P = 0$ and the PS matching network coincides with the S one. The normalized link efficiency, parametrized with respect to Q_{Rx}, is plotted in Figure 3d; the behavior is similar to SP, reaching a high link efficiency for a wide range of R_L, but it performs better for heavy loads, close to R_{Rx}. Figure 3f shows the optimal values of C_S and C_P that allow the maximum efficiency as a function of the load resistance. It is worth noting that they are independent of the Rx quality factor.

3.5. Fixed vs. Adaptive Matching Networks

In WPT systems where the load condition is fixed or does not vary that much, the design criteria described above for both SP and PS MNs represent a useful approach to optimize the MN for the specific load, thus maximizing the link efficiency. Even under varying load conditions, a possible approach is to optimize a fixed MN for the heaviest load envisaged by the application. It is indeed true that maximizing the link efficiency for the heaviest load guarantees that, in any other lighter condition, the transmitted power will always be lower [29]. Therefore, if SAR exposure is guaranteed even with the smallest load resistance, then it will still be guaranteed in all other conditions. However, there are several real case scenarios where the power required by the load can be very high but for very short periods, such that the approach previously described becomes very inefficient.

The best solution to pursue the maximum power transfer under varying loading conditions is an adaptive SP/PS matching network that dynamically updates the value of C_S and C_P according to the power required by the load, tracking the maximum power efficiency. Banks of Series/Parallel capacitors connected by means of controlled switches driven by mixed-signal feedback loops is the typical approach present in the literature [24,30–32].

Regardless of the kind of MN (fixed/adaptive, PS/SP), an LMF technique can be implemented on the Rx side to transmit back information to the Tx side with regard to the amount of received power. In Section 4, we will provide more insights into the design methodology of the back telemetry and a comparison of its effectiveness in fixed and adaptive MNs.

4. LMF with Adaptive Matching Network

There could be several strategies for implementing the LMF [9–11]. A simple way to implement Amplitude Shift Keying (ASK) while preserving the link efficiency $\overline{\eta_{link}}$ is to apply only a variation in the imaginary part of Z_{MN} with respect to Z_{MNopt} (obtained thanks to a PS/SP MN derived in Section 3). Figure 4 shows $\overline{\eta_{link}}/X$ and MD/X for a sweep of $Im\{Z_{MN2}\}$, when $Re\{Z_{MN2}\}$ is left unchanged with respect to the real part of $Z_{MN1} = Z_{MNopt}$. It is easily recognizable that for $Im\{Z_{MN2}\} = -Q_{Rx}R_{Rx}$, we would have $Z_{MN2} = Z_{MNopt}$ and consequently the maximum link efficiency, but no modulation (since $Z_{MN2} = Z_{MN1}$). As expected, moving on from that point, MD increases at the cost of a lower average link efficiency. It is worth mentioning that Figure 4 is independent of the kind of matching network employed on the Rx side or the specific implementation of the load modulation, but it is based only on the assumption that Z_{MN} vary between the two phases as previously described, besides the hypothesis of loose coupling condition ($X \ll 1$).

At this point, we need to implement the variation in the imaginary part of Z_{MN}, leaving the real part unchanged. Thanks to the PS/SP MNs, it is possible to achieve this condition. However, this would require changing both C_S and C_P, complicating the LMF modulator control. For this reason, we investigated the possibility of implementing LMF by means of the modulation of only the parallel capacitor C_P in PS MNs, as shown in Figure 5a. The value of C_S and C_P is sized to obtain $Z_{MN1} = Z_{MNopt}$ (as described in Section 3.4) for the heaviest load (fixed MN) or for varying load conditions (adaptive MN). During one of the two phases, an additional capacitor $C_M \ll C_{RES}$ was added in parallel to C_P, obtaining the following approximated expression:

$$Z_{MN2} \cong \frac{R_{Rx} - j\frac{Q_{Rx}R_{Rx}}{1+\frac{C_M}{C_{RES}}}\left[1 + \frac{R_L}{R_{Rx}Q_{Rx}^2}\left(1 - \sqrt{\frac{R_{Rx}}{R_L}}\right)\right]}{1 + \frac{R_L}{R_{Rx}Q_{Rx}^2}\left(1 - \sqrt{\frac{R_{Rx}}{R_L}}\right)^2} \tag{24}$$

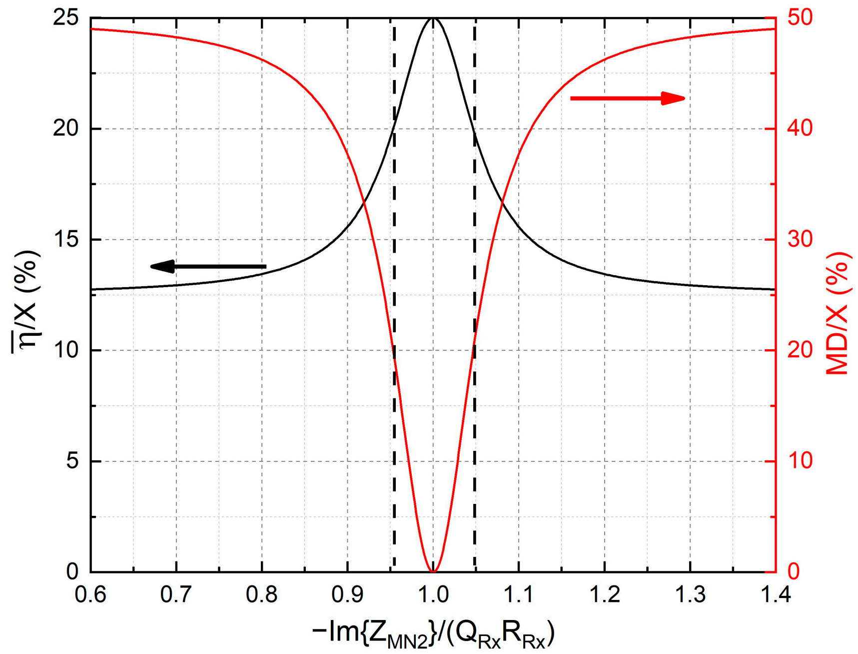

Figure 4. Normalized link efficiency and normalized modulation depth vs. the normalized imaginary part of Z_{MN2} during LMF ($Z_{MN1} = Z_{MNopt}$, Re{Z_{MN2}} = R_{RX}). Dashed lines represent the limits of Im{Z_{MN2}} such that the normalized efficiency is higher than the target value (20%).

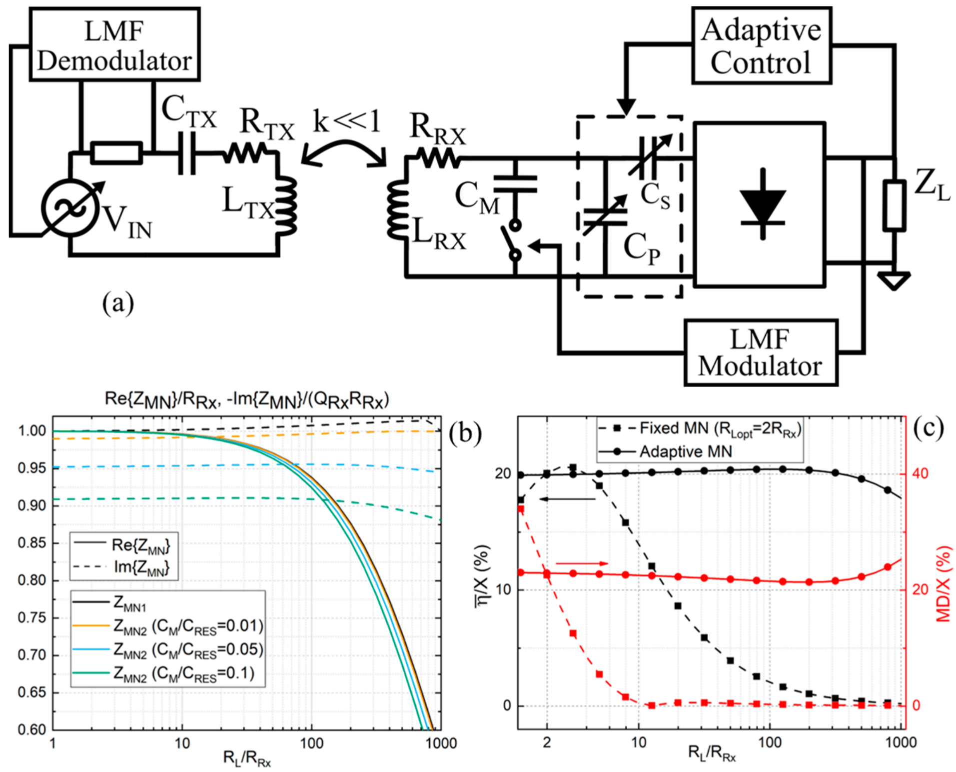

Figure 5. (**a**) Block diagram of studied inductive WPT system, with adaptive control for PS MN and LMF; (**b**) real and imaginary part of Z_{MN} in the presence of LMF with different load conditions for different values of C_M and (**c**) comparison of normalized link efficiency and normalized modulation depth between fixed MN and adaptive MN, with a modulation capacitor $C_M/C_{RES} = 5\%$.

Figure 5b shows the real and the imaginary part of Z_{MN1} and Z_{MN2} for different C_M/C_{RES}. As we can see, the real part of Z_{MN2} does not deviate much from the real part of Z_{MN1} (and only for large loading conditions, where the optimization of the power efficiency is less critical), while the imaginary part decreases monotonically with increasing ratios C_M/C_{RES}, but keeps the same behavior with respect to R_L.

The proposed design procedure for optimizing the link efficiency in the presence of LMF, under loose coupling conditions, is the following: once we have fixed the minimum *MD*, according to the channel noise and the sensitivity of the LMF demodulator (on the Tx side), we can identify the value of C_M by combining the information present in Figures 4 and 5b. For example, if the minimum MD/X is 20%, a ratio $C_M/C_{RES} = 0.05$ entails a 5% variation in the imaginary part of Z_{MN2}, which guarantees the maximum link efficiency for that modulation depth (dashed lines in Figure 4). It is worth remarking that the value of C_M is fixed and will not vary under different operating conditions, thus relaxing the LMF modulator complexity.

Figure 5c shows the normalized link efficiency and the normalized modulation depth for $C_M/C_{RES} = 0.05$ in the case of PS MN, comparing the case of adaptive MN and fixed MN (the latter was designed with C_S and C_P optimized for the largest load, e.g., $R_L = 2R_{Rx}$). It is worth noting that with the adaptive MN, not only do we obtain a larger link efficiency (80% of the maximum achievable one) for a wide load range but we also guarantee a modulation depth higher than the fixed constraint of 20% for three decades of load variations, thus guaranteeing proper communication between Rx and Tx through LMF.

The simulations shown so far were performed with fixed link potential (i.e., fixed coil quality factor and coupling factor) according to the parameters reported in Ref. [11]; in particular, the coupling factor k was set to 1×10^{-3}, which was obtain from the electromagnetic simulations at a distance of 15 cm and perfect alignment between Tx and Rx coils. We investigated a sweep of the coupling factor, from very low values (5×10^{-5}) to higher values (1×10^{-2}), to assess the validity of the proposed design procedure across different working conditions (emulating varying distances and misalignments) and the results are shown in Figure 6. Both the normalized link efficiency and the normalized modulation depth start decreasing at coupling factor values approaching 1×10^{-2}. This is due to the fact that, considering the quality factors of the Tx and Rx coils (respectively, 213 and 35, as derived from [11]), the condition of loose coupling, and in particular the assumption $X \ll 1$, and consequently, the mathematical expressions previously derived, cease to be valid. In any case, this does not represent an issue, since with larger coupling factors, the absolute values of both η and *MD* become larger. For lower values of k, instead, the decrease in the normalized modulation depth is due to simulation inaccuracy in the presence of very small coupling between Tx and Rx. Obviously, such working conditions must be avoided in real case scenarios; otherwise, the risk of losing communication between Rx and Tx due to the presence of noise or the reduced amount of received power is very high. This sets a limit on the maximum distance and misalignment that can be accepted and must be mitigated from a system-level point of view (e.g., by including a 3D Rx coil to reduce the misalignment issues [26] or by optimizing the number and relative position of Tx coils [33]).

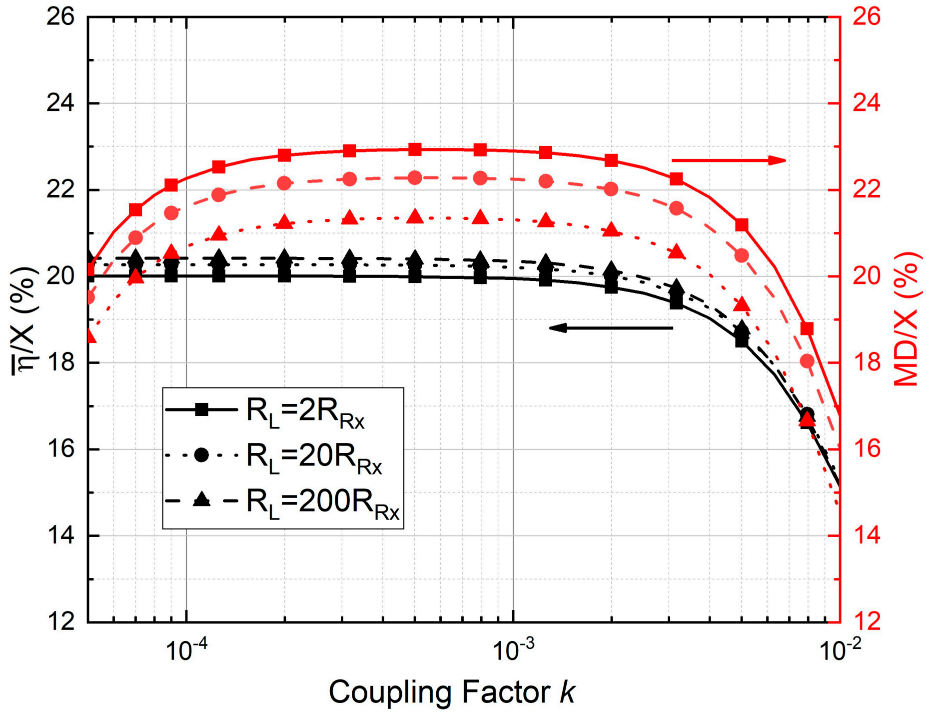

Figure 6. Normalized link efficiency and modulation depth of the proposed WPT system (with adaptive PS MN and LMF performed with a modulation capacitor $C_M/C_{RES} = 5\%$) with respect of the coupling factor k, for three different loading conditions.

5. Conclusions

This paper presented a study of the load modulation feedback technique for wireless power transfer systems in the case of a low-coupling scenario, as is typical of implantable medical devices. A case study of a Parallel–Series adaptive matching network optimized for varying loading conditions, together with a simple yet effective modulation of the parallel capacitor, is illustrated. The simulation results show not only that the adaptive matching network with load modulation feedback achieves high power efficiency but more importantly that the modulation depth on the Tx side is kept almost constant over a wide load range. Compared with other state-of-the-art LMF approaches such as [20,34], where the load modulation is simply achieved by shorting the Rx coil, the proposed approach allows for reaching a better trade-off between modulation depth and link efficiency, at the cost of a relatively small increase in circuital complexity, if joined together with the implementation of the adaptive matching networks.

Besides a specific case study, this paper provided a theoretical framework for studying and optimizing inductive wireless power transfer systems under loose coupling conditions: we derived handy yet effective mathematical expressions of the link efficiency and the modulation depth in the presence of load modulation feedback. The proposed approach is independent of the kind of matching network topology used or the modulation. Overall, this study sheds light on the potential of enhancing the performance and stability of battery-less implantable medical devices.

Author Contributions: Conceptualization, M.B., A.C., G.B., S.S. and G.I.; methodology, M.B.; software, A.C.; validation, S.S.; formal analysis, A.C.; investigation, M.B., G.B. and S.S.; resources, G.I.; data curation, G.B. and S.S.; writing—original draft preparation, M.B. and A.C.; writing—review and editing, S.S. and G.I.; supervision, G.I.; project administration, G.I.; funding acquisition, G.I. All authors have read and agreed to the published version of the manuscript.

Funding: This research was funded by the European Commission through the Horizon 2020 Research and Innovation Programme, under GA AUTOCAPSULE (contract n.952118) and by the MIUR through the Departments on Excellence project FORELAB.

Data Availability Statement: No new data were created or analyzed in this study. Data sharing is not applicable to this article.

Conflicts of Interest: The authors declare no conflict of interest.

References

1. Joung, Y.H. Development of Implantable Medical Devices: From an Engineering Perspective. *Int. Neurourol. J.* **2013**, *17*, 98–106. [CrossRef] [PubMed]
2. Ciuti, G.; Menciassi, A.; Dario, P. Capsule Endoscopy: From Current Achievements to Open Challenges. *IEEE Rev. Biomed. Eng.* **2011**, *4*, 59–72. [CrossRef] [PubMed]
3. Zhou, Y.; Liu, C.; Huang, Y. Wireless Power Transfer for Implanted Medical Application: A Review. *Energies* **2020**, *13*, 2837. [CrossRef]
4. Karimi, M.J.; Schmid, A.; Dehollain, C. Wireless Power and Data Transmission for Implanted Devices via Inductive Links: A Systematic Review. *IEEE Sens. J.* **2021**, *21*, 7145–7161. [CrossRef]
5. Van Mulders, J.; Delabie, D.; Lecluyse, C.; Buyle, C.; Callebaut, G.; Van der Perre, L.; De Strycker, L. Wireless Power Transfer: Systems, Circuits, Standards, and Use Cases. *Sensors* **2022**, *22*, 5573. [CrossRef] [PubMed]
6. Norton, J.C.; Slawinski, P.R.; Lay, H.S.; Martin, J.W.; Cox, B.F.; Cummins, G.; Desmulliez, M.P.Y.; Clutton, R.E.; Obstein, K.L.; Cochran, S.; et al. Intelligent Magnetic Manipulation for Gastrointestinal Ultrasound. *Sci. Robot.* **2019**, *4*, eaav7725. [CrossRef]
7. Abaravcius, B.; Moldovan, A.; Mitra, S.; Cochran, S. Towards Integrated Microultrasound Systems. In Proceedings of the IEEE International Ultrasonics Symposium, IUS, Venice, Italy, 10–13 October 2022; IEEE Computer Society: Washington, DC, USA, 2022; Volume 2022-October.
8. Qiu, Y.; Huang, Y.; Zhang, Z.; Cox, B.F.; Liu, R.; Hong, J.; Mu, P.; Lay, H.S.; Cummins, G.; Desmulliez, M.P.Y.; et al. Ultrasound Capsule Endoscopy With a Mechanically Scanning Micro-Ultrasound: A Porcine Study. *Ultrasound Med. Biol.* **2020**, *46*, 796–804. [CrossRef]
9. Autonomous Multimodal Implantable Endoscopic Capsule for the Gastrointestinal Tract. Available online: https://cordis.europa.eu/project/id/952118 (accessed on 30 August 2023).
10. Pérez-Nicoli, P.; Silveira, F.; Ghovanloo, M. *Inductive Links for Wireless Power Transfer*; Springer International Publishing: Cham, Switzerland, 2021; ISBN 978-3-030-65476-4.
11. Bandini, G.; Buffi, A.; Marracci, M.; Tellini, B.; Rizzo, T.; Macucci, M.; Strangio, S.; Iannaccone, G. Electromagnetic Design of an Inductive Wireless Power Transfer System for Endoscopic Capsule. In Proceedings of the IEEE International Instrumentation and Measurement Technology Conference, Kuala Lumpur, Malaysia, 22–25 May 2023; Institute of Electrical and Electronics Engineers Inc.: Piscataway, NJ, USA, 2023; Volume 2023-May.
12. Khan, S.R.; Pavuluri, S.K.; Cummins, G.; Desmulliez, M.P.Y. Miniaturized 3-D Cross-Type Receiver for Wirelessly Powered Capsule Endoscopy. *IEEE Trans. Microw. Theory Tech.* **2019**, *67*, 1985–1993. [CrossRef]
13. *IEC/IEEE 62209-1528:2020 ED1*; Measurement Procedure for the Assessment of Specific Absorption Rate of Human Exposure to Radio Frequency Fields from Hand-Held and Body-Mounted Wireless Communication Devices—Human Models, Instrumentation, and Procedures (Frequency Range of 4 MHz to 10 GHz). International Electrotechnical Commission (IEC): Geneva, Switzerland, 2020; ISBN 9782832285336.
14. Ziegelberger, G.; Croft, R.; Feychting, M.; Green, A.C.; Hirata, A.; d'Inzeo, G.; Jokela, K.; Loughran, S.; Marino, C.; Miller, S.; et al. Guidelines for Limiting Exposure to Electromagnetic Fields (100 KHz to 300 GHz). *Health Phys.* **2020**, *118*, 483–524.
15. Catrysse, M.; Hermans, B.; Puers, R. An Inductive Power System with Integrated Bi-Directional Data-Transmission. *Sens. Actuators A Phys.* **2004**, *115*, 221–229. [CrossRef]
16. Jiang, D.; Cirmirakis, D.; Schormans, M.; Perkins, T.A.; Donaldson, N.; Demosthenous, A. An Integrated Passive Phase-Shift Keying Modulator for Biomedical Implants with Power Telemetry over a Single Inductive Link. *IEEE Trans. Biomed. Circuits Syst.* **2017**, *11*, 64–77. [CrossRef] [PubMed]
17. Kim, M.; Lee, H.S.; Ahn, J.; Lee, H.M. A 13.56-MHz Wireless Power and Data Transfer System With Current-Modulated Energy-Reuse Back Telemetry and Energy-Adaptive Voltage Regulation. *IEEE J. Solid-State Circuits* **2023**, *58*, 400–410. [CrossRef]
18. Stoecklin, S.; Yousaf, A.; Gidion, G.; Reindl, L.; Rupitsch, S.J. Simultaneous Power Feedback and Maximum Efficiency Point Tracking for Miniaturized Rf Wireless Power Transfer Systems. *Sensors* **2021**, *21*, 2023. [CrossRef]
19. Hannan, M.A.; Abbas, S.M.; Samad, S.A.; Hussain, A. Modulation Techniques for Biomedical Implanted Devices and Their Challenges. *Sensors* **2012**, *12*, 297–319. [CrossRef]
20. Jia, Y.; Mirbozorgi, S.A.; Zhang, P.; Inan, O.T.; Li, W.; Ghovanloo, M. A Dual-Band Wireless Power Transmission System for Evaluating Mm-Sized Implants. *IEEE Trans. Biomed. Circuits Syst.* **2019**, *13*, 595–607. [CrossRef] [PubMed]
21. Rizzo, T.; Catania, A.; Bertolacci, G.; Strangio, S.; Iannaccone, G. A 6.78 MHz Maximum Efficiency Tracking Active Rectifier with Load Modulation Control for Wireless Power Transfer to Implantable Medical Devices. In Proceedings of the ICECS 2022—29th IEEE International Conference on Electronics, Circuits and Systems, Glasgow, UK, 24–26 October 2022; Institute of Electrical and Electronics Engineers Inc.: Piscataway, NJ, USA, 2022.
22. Ahn, D.; Kim, S.; Moon, J.; Cho, I.K. Wireless Power Transfer With Automatic Feedback Control of Load Resistance Transformation. *IEEE Trans. Power Electron.* **2016**, *31*, 7876–7886. [CrossRef]

23. Agarwal, K.; Jegadeesan, R.; Guo, Y.X.; Thakor, N.V. Wireless Power Transfer Strategies for Implantable Bioelectronics. *IEEE Rev. Biomed. Eng.* **2017**, *10*, 136–161. [CrossRef]
24. Lim, Y.; Tang, H.; Lim, S.; Park, J. An Adaptive Impedance-Matching Network Based on a Novel Capacitor Matrix for Wireless Power Transfer. *IEEE Trans. Power Electron.* **2014**, *29*, 4403–4413. [CrossRef]
25. Namgoong, G.; Choi, E.; Park, W.; Lee, B.; Park, H.; Ma, H.; Bien, F. A 6.78 MHz, 95.0% Peak Efficiency Monolithic Two-Dimensional Calibrated Active Rectifier for Wirelessly Powered Implantable Biomedical Devices. *IEEE Trans. Biomed. Circuits Syst.* **2021**, *15*, 509–521. [CrossRef]
26. Carta, R.; Puers, R. Wireless Power and Data Transmission for Robotic Capsule Endoscopes. In Proceedings of the 18th IEEE Symposium on Communications and Vehicular Technology in the Benelux (SCVT), Ghent, Belgium, 22–23 November 2011.
27. Yehui, H.; Perreault, D.J. Analysis and Design of High Efficiency Matching Networks. *IEEE Trans. Power Electron.* **2006**, *21*, 1484–1491. [CrossRef]
28. Kim, C.; Ha, S.; Park, J.; Akinin, A.; Mercier, P.P.; Cauwenberghs, G. A 144-MHz Fully Integrated Resonant Regulating Rectifier with Hybrid Pulse Modulation for Mm-Sized Implants. *IEEE J. Solid-State Circuits* **2017**, *52*, 3043–3055. [CrossRef]
29. De Vita, G.; Iannaccone, G. Design Criteria for the RF Section of UHF and Microwave Passive RFID Transponders. *IEEE Trans. Microw. Theory Tech.* **2005**, *53*, 2978–2990. [CrossRef]
30. Alibakhshikenari, M.; Virdee, B.S.; Shukla, P.; See, C.H.; Abd-Alhameed, R.A.; Falcone, F.; Limiti, E. Improved Adaptive Impedance Matching for RF Front-End Systems of Wireless Transceivers. *Sci. Rep.* **2020**, *10*, 14065. [CrossRef]
31. Lauder, D.; Sun, Y. Design Considerations of Antennas and Adaptive Impedance Matching Networks for RF Energy Harvesting. In Proceedings of the 2020 European Conference on Circuit Theory and Design (ECCTD), Sofia, Bulgaria, 7–10 September 2020; IEEE: Piscataway, NJ, USA, 2020; pp. 1–4. [CrossRef]
32. Cho, J.H.; Lee, B.H.; Kim, Y.J. Maximizing Transfer Efficiency with an Adaptive Wireless Power Transfer System for Variable Load Applications. *Energies* **2021**, *14*, 1417. [CrossRef]
33. Zhang, X.; Lu, X.; Zhang, X.; Wang, L. A Novel Three-Coil Wireless Power Transfer System and Its Optimization for Implantable Biomedical Applications. *Neural Comput. Appl.* **2020**, *32*, 7069–7078. [CrossRef]
34. Lo, Y.K.; Kuan, Y.C.; Culaclii, S.; Kim, B.; Wang, P.M.; Chang, C.W.; Massachi, J.A.; Zhu, M.; Chen, K.; Gad, P.; et al. A Fully Integrated Wireless SoC for Motor Function Recovery after Spinal Cord Injury. *IEEE Trans. Biomed. Circuits Syst.* **2017**, *11*, 497–509. [CrossRef]